

Percolative supercurrent in superconductor-ferromagnetic insulator bilayers

A. Maiani,^{1,2,*} A. C. C. Drachmann,^{1,*} L. Galletti,¹ C. Schrade,³ Y. Liu,¹ R. Seoane Souto,^{1,4,5} and S. Vaitiekėnas¹

¹*Center for Quantum Devices, Niels Bohr Institute,
University of Copenhagen, DK-2100 Copenhagen, Denmark*

²*Nordita, KTH Royal Institute of Technology and Stockholm University,
Hannes Alfvéns väg 12, SE-10691 Stockholm, Sweden*

³*Hearne Institute of Theoretical Physics, Department of Physics & Astronomy,
Louisiana State University, Baton Rouge LA 70803, USA*

⁴*Division of Solid State Physics and NanoLund, Lund University, S-22100 Lund, Sweden*

⁵*Instituto de Ciencia de Materiales de Madrid (ICMM),
Consejo Superior de Investigaciones Científicas (CSIC),
Sor Juana Inés de la Cruz 3, 28049 Madrid, Spain*

(Dated: May 2, 2024)

We report tunneling spectroscopy and transport measurements in superconducting Al and ferromagnetic-insulator EuS bilayers. The samples display remanent spin-splitting, roughly half the superconducting gap, and supercurrent transport above the average paramagnetic limit. We interpret this behavior as arising from the interplay between two characteristic length scales: the superconducting coherence length, ξ , and the magnetic domain size, d . By comparing experimental results to a theoretical model, we find $\xi/d \approx 10$. In this regime, spin-averaging across the micro-magnetic configuration can locally suppress superconductivity, resulting in percolative supercurrent flow.

The coexistence of superconducting pairing and ferromagnetic ordering typically leads to intriguing ground states, emerging from the competing electrical properties [1, 2]. Predicted manifestations include proximity-induced spin-splitting [3–5], spatial modulation of the order parameter [6, 7], and the onset of unconventional superconducting pairing state [8, 9]. These phenomena play a key role in designing current-phase relation in hybrid Josephson junctions [10–13], superconducting diodes [14–16], and thermoelectric devices [17–19]. Controlling the interplay between these orders enables the synthesis of spin-orbit interactions [20–22], spin-triplet pairing [23–25], and topological superconductivity [26–34].

In pristine superconductor-ferromagnetic-insulator heterostructures, interfacial scattering can induce strong exchange splitting, h , with little contribution from stray fields [35–37]. For homogeneous samples at low temperatures, the superconducting order parameter, Δ , depends weakly on h but gets fully suppressed at the paramagnetic limit, h_C [38]. At zero temperature, the transition to the normal state is first order, occurring at a critical splitting $h_{C0} = \Delta/\sqrt{2}$, known as the Chandrasekhar-Clogston limit [39, 40]. As the temperature increases, the critical field decreases, and the transition becomes second-order [41].

At a given point within the superconductor, the induced h is proportional to the local micromagnetic domain configuration, \mathbf{m} , averaged over a characteristic spin-averaging length, ξ [42, 43]. At low energies, ξ is dominated by superconducting correlations and corresponds to the superconducting coherence length [35, 44]. Under non-equilibrium conditions, ξ is renormalized due to quasiparticle diffusion [45, 46]. For samples with a minimal magnetic domain size $d \ll \xi$, the ferromagnetic

proximity effect weakens superconductivity through spin-flip scattering [47], while the induced exchange splitting approximately homogeneous and approaches the sample-average $\langle h \rangle$ [48, 49]. For $d \gg \xi$, the superconductivity can be suppressed locally but persists at the domain boundaries [50, 51], as has been observed, for instance, in heterostructures with out-of-plane magnetization [52–54]. Several previous experiments on superconductor-ferromagnetic-insulator bilayers reported measurements compatible with the $d \gg \xi$ case [55–58].

Here, we investigate superconducting Al and the ferromagnetic-insulator EuS bilayers using two complementary experimental techniques. Tunneling spectroscopy reveals hysteretic superconductivity characterized by a remanent $h \approx 130 \mu\text{eV}$ at zero field, nearly half the superconducting gap $\Delta = 280 \mu\text{eV}$, and negligible spin-splitting at the coercive field. This highlights the importance of the spin-averaging effects in our samples. Resistance measurements on proximitized Al bars show h_C that increases with bar width, eventually surpassing the paramagnetic limit. A simple resistive-network model suggests this behavior stems from supercurrent percolation around normal regions in the sample. By fitting the model, we estimate $\xi/d \approx 10$, contrasting with previous experiments on similar bilayers.

Measurements were performed on an Al/EuS (5/10 nm) bilayer grown on an insulating Si substrate. The Al bars were lithographically defined using selective wet etch. Tunneling junctions were formed by metalizing strips of Ti/Au (3/20 nm) across selected Al bars, using the native AlOx (3 nm) as the barrier; see Figs. 1(a) and 1(b). Two samples with several devices each showed consistent results. In the main text, we report representative data from Sample 1. Supporting data from other devices are

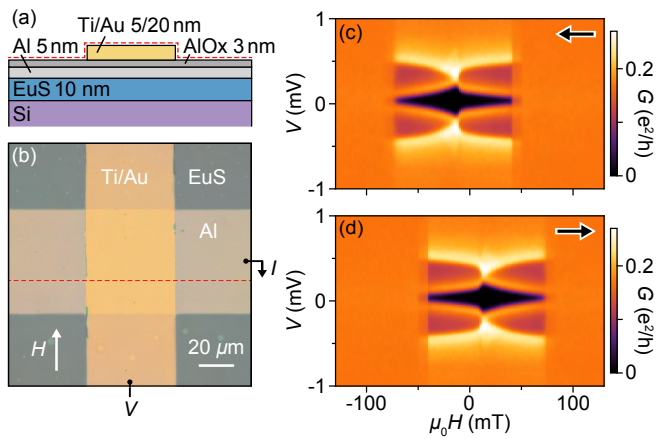


FIG. 1. (a) Schematic cross-section of Al-EuS bilayer with a Ti/Au lead on top of native AlOx layer, used for tunneling spectroscopy. (b) Optical micrograph of $60 \times 50 \mu\text{m}^2$ junction with measurement setup. (c) and (d) Differential conductance, G , as a function of voltage bias, V , and in-plane magnetic field, H , measured for the junction shown in (b), sweeping H from (b) positive to negative and (c) negative to positive. The spectra display a superconducting gap with sweep-direction-dependent evolution of the coherence peak splitting. The data were taken after polarizing the sample at $\mu_0 H_{\parallel} = \pm 200$ mT.

summarized in the Supplemental Material [59]. Standard ac lock-in techniques were used in a dilution refrigerator with a three-axis vector magnet and base electron temperature of 40 mK.

We begin with tunneling spectroscopy of the junctions. Differential conductance, $G = dI/dV$, measured for a $60 \times 50 \mu\text{m}^2$ junction as a function of voltage bias, V , shows a hysteretic evolution with an in-plane magnetic field, H [Figs. 1(c) and 1(d)]. Starting at $\mu_0 H = 200$ mT, the junction displays a featureless $G(V)$. Decreasing the field toward zero, the conductance spectrum becomes gapped at $\mu_0 H \approx 40$ mT, showing split peaks positioned symmetrically around $V = 0$. The splitting decreases as the field passes through zero, becoming negligible around $\mu_0 H = -15$ mT, where the spectral gap is maximal. The peaks gradually split again for more negative H and the spectrum turns featureless at $\mu_0 H \approx 70$ mT. An inverse behavior is observed when sweeping from negative to positive H .

The measured tunneling spectra resemble the superconducting density of states with spin-split coherence peaks. The nonlinear and hysteretic response to the external field can be attributed to the proximity-induced exchange coupling. The separation between the coherence peaks provides a measure of the sample-average exchange splitting. In our sample, the peaks merge around $\mu_0 H = \pm 15$ mT, which we associate with the coercive field of the ferromagnetic insulator, implying that a typical magnetic domain is smaller than the spin-averaging length. The transition to a normal state at higher magnetic fields can be un-

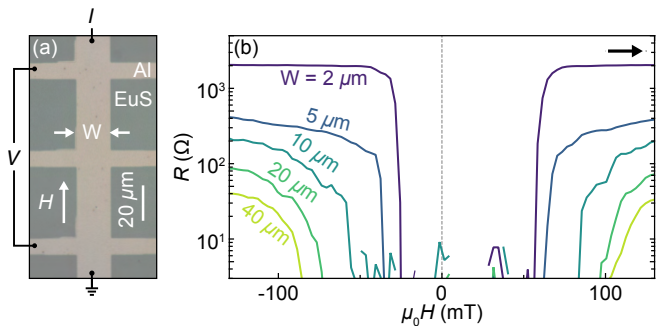


FIG. 2. (a) Optical micrograph of $20 \mu\text{m}$ wide Al bar showing the four-probe measurement setup. (b) Differential resistance, R , as a function of in-plane magnetic field, H , measured for Al bars of different widths, showing a superconducting window centered away from $H = 0$. The onset of the resistive state increases with bar width.

derstood by domain magnetization, yielding an average induced splitting larger than the paramagnetic limit. We note that the transition is gradual, with an intermediate state showing smeared features [see Figs. 1(c) and 1(d)], suggesting that superconductivity can survive locally where the induced exchange splitting is below the paramagnetic limit.

We next investigate supercurrent transport in proximitized Al bars [Fig. 2(a)]. Four-terminal differential resistance, $R = dV/dI$, measured as a function of H for Al bars of varying widths from 2 to $40 \mu\text{m}$ reveals a hysteretic window of suppressed resistance; see Fig. 2(b). The size of the window displays a characteristic dependence on the bar width, spanning ≈ 100 mT for the narrower bars, similar to the gapped region identified in the junctions. In contrast, for the wider bars, the window broadens, extending to nearly 200 mT for $40 \mu\text{m}$ Al bar, with the onset of the resistive state at $\mu_0 H \approx 100$ mT exceeding the paramagnetic limit measured from the tunneling spectroscopy. We note that the transition to the resistive state is gradual for all widths, but becomes progressively smoother for wider bars.

The observed behavior can be interpreted as the magnetization-driven superconductor-normal metal transition. Resistance remains suppressed as long as there is a superconducting path along the bar, allowing for current to flow without dissipation. With increasing H , the domains form clusters with uniform magnetization that suppress superconductivity locally, and the percolative supercurrent paths get interrupted by normal regions, leading to finite R . In this regime, R depends on the length of the normal regions the current passes. For larger H , the magnetization drives the whole sample normal, and R saturates; see Fig. 2(b). At a given H , the supercurrent percolation is more likely to be interrupted in a narrow bar than in a wider one.

To support our interpretation, we introduce a theoretical framework that uses experimentally measured param-

eters to model supercurrent transport in bars of different widths. First, we extract the global average exchange splitting, $\langle h \rangle$, and the superconducting gap, Δ , by numerically fitting the tunneling spectroscopy data [Figs. 1(c) and 1(d)] to the nonlinear Usadel model [60]. The conductance can be expressed as

$$G(V) = G_N[1 - x_N]n_S(eV) + G_Nx_N, \quad (1)$$

where G_N is the normal state differential conductance, $x_N \simeq G(V=0)/G_N$ is the fraction of the sample in the normal state, and n_S is the thermally broadened superconducting density of states described by the homogeneous Usadel equations that include average exchange splitting [8, 19, 38]. The output of the Usadel fit procedure is summarized in Figs. 3(a) and 3(b). A more detailed description of the model, fitting procedure, and results are given in the Supplemental Material [59] and Ref. [61].

We proceed by considering the spatial distribution of the exchange splitting and its dependence on the local magnetic domain configuration. The ferromagnetic insulator is modeled as a grid of magnetic grains, each of size d , that are constrained to align either parallel or antiparallel to the external magnetic field. The proximity-induced local exchange splitting is described as

$$\langle \mathbf{h} \rangle_\xi = h_S \langle \mathbf{m} \rangle_\xi + g\mu_B\mu_0\mathbf{H}/2, \quad (2)$$

where h_S is the saturation exchange splitting that defines the strength of the proximity effect, $\langle \mathbf{m} \rangle_\xi = \mathbf{m}(\mathbf{r}) \otimes K_\xi(\mathbf{r})$ is effective domain configuration acting on a point averaged over ξ using filter K_ξ , as described in Ref. [59], $g = 2$ is the electron g factor, μ_B is the Bohr magneton, and $\mu_0\mathbf{H}$ is the external magnetic field. We stress that the local average exchange field $\langle \mathbf{h} \rangle_\xi$ is an inhomogeneous quantity in contrast with the global average $\langle \mathbf{h} \rangle$ that takes a single value for a given domain configuration.

To apply the model to the experimental data, we first estimate the sample average magnetization, $M(H)$, by fitting the extracted exchange splitting to a double hyperbolic tangent function [62]

$$M(H) = M_S \frac{\sum_{i=1,2} C_i \tanh[N_i(H \pm H_C)]}{\sum_{i=1,2} C_i}, \quad (3)$$

where M_S is the saturation magnetization defined as $M/M_S = \langle \mathbf{m} \rangle$, whereas C_i , N_i , and H_C are the amplitude, scaling, and coercive-field fit parameters, respectively; see solid curves in Fig. 3(d). The magnetization curve is then compared to the model by generating a randomized evolution of the micromagnetic configuration $\mathbf{m}(H)$, whose average reproduces the extracted $M(H)/M_S$. We assume that superconductivity is suppressed at points where the local exchange field, $\langle \mathbf{h} \rangle_\xi$, calculated using Eq. (2), exceeds the Chandrasekhar-Clogston limit, $h_{C0} = \Delta/\sqrt{2} = (198 \pm 3) \mu\text{eV}$, with average Δ taken from the fit in Fig. 2(b). With this,

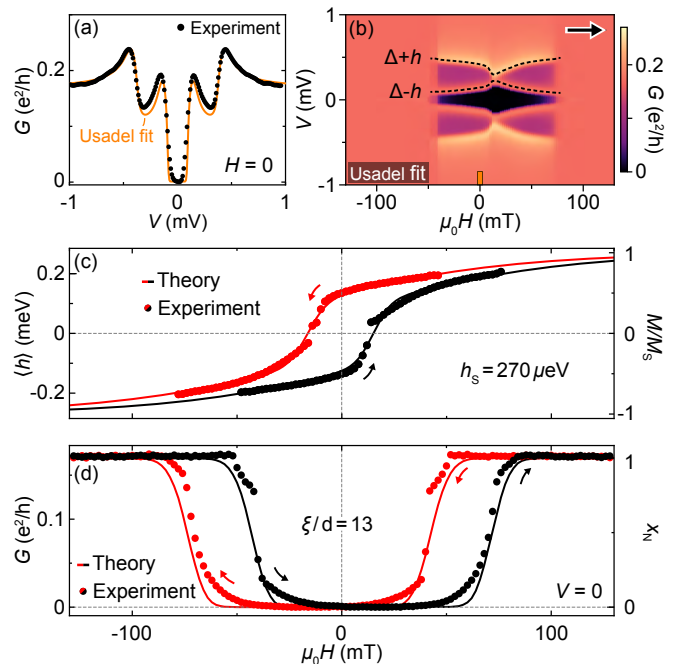


FIG. 3. (a) Differential conductance, G , as a function of voltage bias, V , measured for $60 \times 50 \mu\text{m}^2$ junction at zero in-plane magnetic field, $H = 0$, (data points) and Usadel model fit (solid curve). (b) Usadel model fit applied to the data in Fig. 2(d). The extracted mean superconducting gap, $\Delta = 280 \mu\text{eV}$. (c) Extracted sample-averaged exchange field, $\langle h \rangle$, (data points) and extrapolated magnetization curve, M , (solid curves) normalized to its saturation value, M_S , giving a saturation exchange splitting of $h_S = 270 \mu\text{eV}$. (d) Comparison of zero-bias conductance measured as a function H (data points) with the fraction of the sample in the normal state, x_N , (solid curves) calculated using the ratio between superconducting coherence length and magnetic domain size, $\xi/d = 13$.

the predicted normal metal fraction, x_N , is given by the average number of normal regions. We estimate the values of $h_S = (270 \pm 10) \mu\text{eV}$ and $\xi/d = 13 \pm 3$ by fitting the experimental zero-bias differential conductance to the predicted x_N ; see Fig. 3(d).

Finally, we use a resistive network model to simulate the supercurrent transport in proximitized Al bars. We follow the same procedure as in the previous step to generate $\mathbf{m}(H)$ for a grid of $W \times L$ domains. For each value of H , the resistance of the bar can be calculated by assigning a finite resistivity $\rho_N = 40 \Omega\Box$, taken from Fig. 2(b), to the normal regions and $\rho_S = 0$ to the superconducting regions and solving the continuity equation for the current [59]. We assume strong coupling between the superconducting regions and, therefore, neglect the phase dynamic that may be relevant for very narrow superconducting constrictions [63]. In the normal state, the bar resistance saturates at $\rho_N L/W$. The simulated resistance for grids with a fixed $L = 1000d$ displays a hysteretic superconducting window that increases with W , quali-

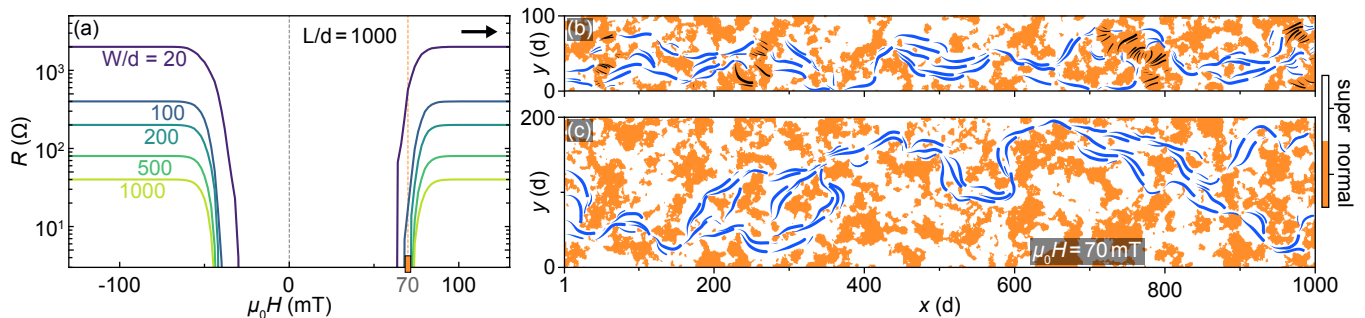


FIG. 4. (a) Calculated resistance, R , as a function of the applied magnetic field, H , for grids of $W \times L$ domains. The onset of R increases with W . (b) Simulated distribution of superconducting (white) and normal (orange) regions for a grid with $W/d = 100$ and $L/d = 1000$ at $\mu_0 H_{\parallel} = 70$ mT, overlaid with a stream plot that illustrates the paths of supercurrent (blue) and normal current (black). Note that several normal regions span the entire width of the grid, disrupting the supercurrent flow. (c) Similar to (b) but for $W/d = 200$, showing uninterrupted supercurrent percolation along the grid.

tatively reproducing the experimental observations; see Fig. 4(a).

To better understand this behavior, we compare the distribution of superconducting and normal regions at the onset of the resistive state, simulated for two bars with $W = 100d$ and $200d$; see Figs. 4(b) and 4(c). At $\mu_0 H = 70$ mT, the narrower bar displays several segments where the normal regions span the entire width [see orange patches in Fig. 4(b)], interrupting supercurrent flow along the bar and causing dissipation. At the same magnetic field, the wider bar exhibits a comparable density of normal regions but none that extends across the full width. In this case, the supercurrent can percolate around the normal regions, allowing for dissipationless current flow. We note that while the precise magnetic field value for the onset of the resistive state is inherently random, it strongly depends on both W and L . For a fixed length, narrower bars are more susceptible to supercurrent interruptions due to the presence of normal regions.

Our resistive network model disregards the Δ dependence on h , which may lead to an increase in ξ close to the paramagnetic limit. Furthermore, while the simulated grids maintain the aspect ratios of the experimental Al bars, they are scaled down because of computational constraints. These simplifications could explain the quantitative differences between the experimental [Fig. 2(b)] and simulated [Fig. 4(a)] resistance traces.

In summary, we have studied superconducting Al and ferromagnetic-insulator EuS bilayers using two experi-

mental techniques. Tunneling from a normal lead into the proximitized Al showed hysteretic superconducting spectra with sizable remanent spin-splitting. Current transport in Al bars revealed a hysteretic superconducting window that broadened in the applied field as device width increased. We argue that this behavior is driven by the interplay between two characteristic length scales: the superconducting coherence length and the magnetic domain size. To support this interpretation, we introduce a theoretical framework suggesting that the superconducting coherence length is roughly ten times longer than a typical magnetic domain size. Using the extracted parameters, we explain our observation in terms of supercurrent percolation around extended normal regions in the sample.

We thank Karsten Flensberg and Charles Marcus for valuable discussions, Peter Krogstrup and Claus Sørensen for contributions to materials growth. We acknowledge support from the Danish National Research Foundation, the Danish Council for Independent Research [Natural Sciences, European Research Council (Grant Agreement No. 856526), European Innovation Council (Grant Agreement No. 101115548), Spanish CM “Talento Program” (project No. 2022-T1/IND-24070), Spanish Ministry of Science, Innovation, and Universities through Grants PID2022-140552NA-I00, NanoLund, and a research grant (Project 43951 and 53097) from VILLUM FONDEN.

orbit scattering, *Phys. Rev. B* **11**, 4224 (1975).

* These authors contributed equally to this work.

- [1] R. Meservey and P. Tedrow, Spin-polarized electron tunneling, *Phys. Rep.* **238**, 173 (1994).
- [2] A. I. Buzdin, Proximity effects in superconductor-ferromagnet heterostructures, *Rev. Mod. Phys.* **77**, 935 (2005).
- [3] R. Meservey, P. M. Tedrow, and R. C. Bruno, Tunneling measurements on spin-paired superconductors with spin-

- [4] Y. M. Xiong, S. Stadler, P. W. Adams, and G. Catelani, Spin-Resolved Tunneling Studies of the Exchange Field in EuS/Al Bilayers, *Phys. Rev. Lett.* **106**, 247001 (2011).
- [5] F. Hübner, M. J. Wolf, T. Scherer, D. Wang, D. Beckmann, and H. v. Löhneysen, Observation of Andreev Bound States at Spin-active Interfaces, *Phys. Rev. Lett.* **109**, 087004 (2012).
- [6] P. Fulde and R. A. Ferrell, Superconductivity in a strong spin-exchange field, *Phys. Rev.* **135**, A550 (1964).
- [7] A. I. Larkin and Y. N. Ovchinnikov, Nonuniform state of

- superconductors, *Zh. Eksp. Teor. Fiz.* **47**, 1136 (1964).
- [8] F. S. Bergeret, A. F. Volkov, and K. B. Efetov, Odd triplet superconductivity and related phenomena in superconductor-ferromagnet structures, *Rev. Mod. Phys.* **77**, 1321 (2005).
- [9] D. Seleznyov, V. Yagovtsev, N. Pugach, and L. Tao, Ferromagnetic insulator induced inverse proximity effect in superconducting dos, *J. Magn. Magn. Mater.* , 171645 (2023).
- [10] H. Sellier, C. Baraduc, F. Lefloch, and R. Calemczuk, Half-integer shapiro steps at the $0-\pi$ crossover of a ferromagnetic josephson junction, *Phys. Rev. Lett.* **92**, 257005 (2004).
- [11] E. Strambini, F. S. Bergeret, and F. Giazotto, Mesoscopic Josephson junctions with switchable current-phase relation, *EPL* **112**, 17013 (2015).
- [12] D. Razmadze, R. S. Souto, L. Galletti, A. Maiani, Y. Liu, P. Krogstrup, C. Schrade, A. Gyenis, C. M. Marcus, and S. Vaitiekėnas, Supercurrent reversal in ferromagnetic hybrid nanowire Josephson junctions, *Phys. Rev. B* **107**, L081301 (2023).
- [13] A. Maiani, K. Flensberg, M. Leijnse, C. Schrade, S. Vaitiekėnas, and R. S. Souto, Nonsinusoidal current-phase relations in semiconductor–superconductor–ferromagnetic insulator devices, *Phys. Rev. B* **107**, 245415 (2023).
- [14] F. Ando, Y. Miyasaka, T. Li, J. Ishizuka, T. Arakawa, Y. Shiota, T. Moriyama, Y. Yanase, and T. Ono, Observation of superconducting diode effect, *Nature* **584**, 373 (2020).
- [15] E. Strambini, M. Spies, N. Ligato, S. Ilić, M. Rouco, C. González-Orellana, M. Ilyn, C. Rogero, F. S. Bergeret, J. S. Moodera, P. Virtanen, T. T. Heikkilä, and F. Giazotto, Superconducting spintronic tunnel diode, *Nat. Commun.* **13**, 2431 (2022).
- [16] Y. Hou, F. Nichele, H. Chi, A. Lodesani, Y. Wu, M. F. Ritter, D. Haxell, M. Davydova, S. Ilić, O. Glezakou-Elbert, A. Varambally, F. S. Bergeret, A. Kamra, L. Fu, P. A. Lee, and J. S. Moodera, Ubiquitous Superconducting Diode Effect in Superconductor Thin Films, *Phys. Rev. Lett.* **131**, 027001 (2023).
- [17] P. Machon, M. Eschrig, and W. Belzig, Nonlocal Thermoelectric Effects and Nonlocal Onsager relations in a Three-Terminal Proximity-Coupled Superconductor-Ferromagnet Device, *Phys. Rev. Lett.* **110**, 047002 (2013).
- [18] S. Kolenda, M. Wolf, and D. Beckmann, Observation of Thermoelectric Currents in High-Field Superconductor-Ferromagnet Tunnel Junctions, *Phys. Rev. Lett.* **116**, 097001 (2016).
- [19] F. S. Bergeret, M. Silaev, P. Virtanen, and T. T. Heikkilä, Colloquium: Nonequilibrium effects in superconductors with a spin-splitting field, *Rev. Mod. Phys.* **90**, 041001 (2018).
- [20] J. Klinovaja, P. Stano, and D. Loss, Transition from fractional to majorana fermions in rashba nanowires, *Phys. Rev. Lett.* **109**, 236801 (2012).
- [21] M. Kjaergaard, K. Wölms, and K. Flensberg, Majorana fermions in superconducting nanowires without spin-orbit coupling, *Phys. Rev. B* **85**, 020503(R) (2012).
- [22] M. M. Desjardins, L. C. Contamin, M. R. Delbecq, M. C. Dartiailh, L. E. Bruhat, T. Cubaynes, J. J. Viennot, F. Mallet, S. Rohart, A. Thiaville, A. Cottet, and T. Kontos, Synthetic spin–orbit interaction for Majorana devices, *Nat. Mater.* **18**, 1060 (2019).
- [23] J. Linder and A. V. Balatsky, Odd-frequency superconductivity, *Rev. Mod. Phys.* **91**, 045005 (2019).
- [24] M. A. Silaev, I. V. Bobkova, and A. M. Bobkov, Odd triplet superconductivity induced by a moving condensate, *Phys. Rev. B* **102**, 100507(R) (2020).
- [25] S. Diesch, P. Machon, M. Wolz, C. Sürgers, D. Beckmann, W. Belzig, and E. Scheer, Creation of equal-spin triplet superconductivity at the Al/EuS interface, *Nat. Commun.* **9**, 5248 (2018).
- [26] J. D. Sau, R. M. Lutchyn, S. Tewari, and S. Das Sarma, Generic New Platform for Topological Quantum Computation Using Semiconductor Heterostructures, *Phys. Rev. Lett.* **104**, 040502 (2010).
- [27] C. Schrade, A. A. Zyuzin, J. Klinovaja, and D. Loss, Proximity-Induced π Josephson Junctions in Topological Insulators and Kramers Pairs of Majorana Fermions, *Phys. Rev. Lett.* **115**, 237001 (2015).
- [28] S. Vaitiekėnas, Y. Liu, P. Krogstrup, and C. M. Marcus, Zero-bias peaks at zero magnetic field in ferromagnetic hybrid nanowires, *Nat. Phys.* **17**, 43 (2020).
- [29] A. Maiani, R. Seoane Souto, M. Leijnse, and K. Flensberg, Topological superconductivity in semiconductor–superconductor–magnetic-insulator heterostructures, *Phys. Rev. B* **103**, 104508 (2021).
- [30] A. Khindanov, J. Alicea, P. Lee, W. S. Cole, and A. E. Antipov, Topological superconductivity in nanowires proximate to a diffusive superconductor–magnetic-insulator bilayer, *Phys. Rev. B* **103**, 134506 (2021).
- [31] S. D. Escribano, E. Prada, Y. Oreg, and A. L. Yeyati, Tunable proximity effects and topological superconductivity in ferromagnetic hybrid nanowires, *Phys. Rev. B* **104**, L041404 (2021).
- [32] C.-X. Liu, S. Schuwalow, Y. Liu, K. Vilkelis, A. L. R. Manesco, P. Krogstrup, and M. Wimmer, Electronic properties of InAs/EuS/Al hybrid nanowires, *Phys. Rev. B* **104**, 014516 (2021).
- [33] C.-X. Liu and M. Wimmer, Optimizing the topological properties of semiconductor-ferromagnet-superconductor heterostructures, *Phys. Rev. B* **105**, 224502 (2022).
- [34] S. D. Escribano, A. Maiani, M. Leijnse, K. Flensberg, Y. Oreg, A. L. Yeyati, E. Prada, and R. S. Souto, Semiconductor-ferromagnet-superconductor planar heterostructures for 1D topological superconductivity, *npj Quantum Mater.* **7**, 81 (2022).
- [35] T. Tokuyasu, J. A. Sauls, and D. Rainer, Proximity effect of a ferromagnetic insulator in contact with a superconductor, *Phys. Rev. B* **38**, 8823 (1988).
- [36] B. Li, N. Roschewsky, B. A. Assaf, M. Eich, M. Epstein-Martin, D. Heiman, M. Münzenberg, and J. S. Moodera, Superconducting Spin Switch with Infinite Magnetoresistance Induced by an Internal Exchange Field, *Phys. Rev. Lett.* **110**, 097001 (2013).
- [37] Y. Liu, S. Vaitiekėnas, S. Martí-Sánchez, C. Koch, S. Hart, Z. Cui, T. Kanne, S. A. Khan, R. Tanta, S. Upadhyay, M. E. Cachaza, C. M. Marcus, J. Arbiol, K. A. Moler, and P. Krogstrup, Semiconductor–Ferromagnetic Insulator–Superconductor Nanowires: Stray Field and Exchange Field, *Nano Lett.* **20**, 456 (2019).
- [38] T. T. Heikkilä, M. Silaev, P. Virtanen, and F. S. Bergeret, Thermal, electric and spin transport in superconductor/ferromagnetic-insulator structures, *Prog. Surf. Sci.* **94**, 100540 (2019).
- [39] B. S. Chandrasekhar, A note on the maximum critical field of high-field superconductors, *Appl. Phys. Lett.* **1**, 7

- (1962).
- [40] A. M. Clogston, Upper Limit for the Critical Field in Hard Superconductors, *Phys. Rev. Lett.* **9**, 266 (1962).
- [41] G. Sarma, On the influence of a uniform exchange field acting on the spins of the conduction electrons in a superconductor, *J. Phys. Chem. Solids* **24**, 1029 (1963).
- [42] B. T. Matthias and H. Suhl, Possible Explanation of the "Coexistence" of Ferromagnetism and Superconductivity, *Phys. Rev. Lett.* **4**, 51 (1960).
- [43] T. Champel and M. Eschrig, Effect of an inhomogeneous exchange field on the proximity effect in disordered superconductor-ferromagnet hybrid structures, *Phys. Rev. B* **72**, 054523 (2005).
- [44] F. S. Bergeret, A. F. Volkov, and K. B. Efetov, Induced ferromagnetism due to superconductivity in superconductor-ferromagnet structures, *Phys. Rev. B* **69**, 174504 (2004).
- [45] J. P. Morten, A. Brataas, and W. Belzig, Spin transport in diffusive superconductors, *Phys. Rev. B* **70**, 212508 (2004).
- [46] A. Hijano, V. N. Golovach, and F. S. Bergeret, Quasiparticle density of states and triplet correlations in superconductor/ferromagnetic-insulator structures across a sharp domain wall, *Phys. Rev. B* **105**, 174507 (2022).
- [47] R. C. Bruno and B. B. Schwartz, Magnetic Field Splitting of the Density of States of Thin Superconductors, *Phys. Rev. B* **8**, 3161 (1973).
- [48] D. A. Ivanov and Y. V. Fominov, Minigap in superconductor-ferromagnet junctions with inhomogeneous magnetization, *Phys. Rev. B* **73**, 214524 (2006).
- [49] F. Aikebaier, P. Virtanen, and T. Heikkilä, Superconductivity near a magnetic domain wall, *Phys. Rev. B* **99**, 104504 (2019).
- [50] A. Y. Aladyshkin, A. I. Buzdin, A. A. Fraerman, A. S. Mel'nikov, D. A. Ryzhov, and A. V. Sokolov, Domain-wall superconductivity in hybrid superconductor-ferromagnet structures, *Phys. Rev. B* **68**, 184508 (2003).
- [51] Z. Jing, H. Yong, and Y.-H. Zhou, Vortex structures and magnetic domain patterns in the superconductor/ferromagnet hybrid bilayer, *Supercond. Sci. Technol.* **27**, 105005 (2014).
- [52] Z. Yang, M. Lange, A. Volodin, R. Szymczak, and V. V. Moshchalkov, Domain-wall superconductivity in superconductor-ferromagnet hybrids, *Nat. Mater.* **3**, 793 (2004).
- [53] M. Iavarone, S. A. Moore, J. Fedor, S. T. Ciocys, G. Karapetrov, J. Pearson, V. Novosad, and S. D. Bader, Visualizing domain wall and reverse domain superconductivity, *Nat. Commun.* **5**, 4766 (2014).
- [54] A. Stelhorn, A. Sarkar, E. Kentzinger, J. Barthel, A. D. Bernardo, S. Nandi, P. Zakalek, J. Schubert, and T. Brückel, Tailoring superconducting states in superconductor-ferromagnet hybrids, *New J. Phys.* **22**, 093001 (2020).
- [55] E. Strambini, V. N. Golovach, G. De Simoni, J. S. Moodera, F. S. Bergeret, and F. Giazotto, Revealing the magnetic proximity effect in EuS/Al bilayers through superconducting tunneling spectroscopy, *Phys. Rev. Mater.* **1**, 054402 (2017).
- [56] M. Rouco, S. Chakraborty, F. Aikebaier, V. N. Golovach, E. Strambini, J. S. Moodera, F. Giazotto, T. T. Heikkilä, and F. S. Bergeret, Charge transport through spin-polarized tunnel junction between two spin-split superconductors, *Phys. Rev. B* **100**, 184501 (2019).
- [57] A. Hijano, S. Ilić, M. Rouco, C. González-Orellana, M. Ilyn, C. Rogero, P. Virtanen, T. T. Heikkilä, S. Khorshidian, M. Spies, N. Ligato, F. Giazotto, E. Strambini, and F. S. Bergeret, Coexistence of superconductivity and spin-splitting fields in superconductor/ferromagnetic insulator bilayers of arbitrary thickness, *Phys. Rev. Res.* **3**, 023131 (2021).
- [58] P. Machon, M. J. Wolf, D. Beckmann, and W. Belzig, Experimental and theoretical study of field-dependent spin splitting at ferromagnetic insulator-superconductor interfaces, *Beilstein J. Nanotechnol.* **13**, 682 (2022).
- [59] See Supplemental Material for sample preparation and measurement details, theoretical model description, and additional data.
- [60] K. D. Usadel, Generalized Diffusion Equation for Superconducting Alloys, *Phys. Rev. Lett.* **25**, 507 (1970).
- [61] A. Maiani, A. Drachmann, L. Galletti, C. Schrade, Y. Liu, R. Seoane Souto, and S. Vaitiekėnas, Experimental data and simulation code for: Percolative supercurrent in superconductor-ferromagnetic-insulator bilayers, Zenodo, (2024); [10.5281/zenodo.11066029](https://doi.org/10.5281/zenodo.11066029).
- [62] I. Mészáros, Magnetization curve modelling of soft magnetic alloys, *J. Phys: Conf. Ser.* **268**, 012020 (2011).
- [63] V. Kresin, Y. Ovchinnikov, and S. Wolf, Inhomogeneous superconductivity and the "pseudogap" state of novel superconductors, *Phys. Rep.* **431**, 231 (2006).

Supplemental Material:

Percolative supercurrent in superconductor-ferromagnetic insulator bilayers

A. Maiani,^{1,2,*} A. C. C. Drachmann,^{1,*} L. Galletti,¹ C. Schrade,³ Y. Liu,¹ R. Seoane Souto,^{1,4,5} and S. Vaitiekėnas¹

¹*Center for Quantum Devices, Niels Bohr Institute,
University of Copenhagen, DK-2100 Copenhagen, Denmark*

²*Nordita, KTH Royal Institute of Technology and Stockholm University,
Hannes Alfvéns väg 12, SE-10691 Stockholm, Sweden*

³*Hearne Institute of Theoretical Physics, Department of Physics & Astronomy,
Louisiana State University, Baton Rouge LA 70803, USA*

⁴*Division of Solid State Physics and NanoLund, Lund University, S-22100 Lund, Sweden*

⁵*Instituto de Ciencia de Materiales de Madrid (ICMM),
Consejo Superior de Investigaciones Científicas (CSIC),
Sor Juana Inés de la Cruz 3, 28049 Madrid, Spain*

(Dated: May 2, 2024)

SAMPLE PREPARATION

The Al-EuS bilayer studied in this work was prepared on a 2-inch intrinsic (100) FZ Si wafer with resistivity $> 10^4 \Omega \text{ cm}$ (Sil'tronix Silicon Technologies). First, the silicon wafer was etched in a 5% HF solution for 10 s to strip the native oxide. After cleaning, the wafer was loaded into a dedicated metal deposition chamber that is part of a molecular beam epitaxy (MBE) system with a background pressure $< 10^{-10}$ Torr. Both layers were deposited using electron beam evaporation. The 10 nm EuS layer was grown at room temperature with an average growth rate of 0.01 nm/s. Next, the sample was annealed *in situ* for one hour at 400°C, followed by 6 hours of cooling. The 7 nm Al layer was evaporated at a rate of 0.06 nm/s with a nominal substrate temperature of -156°C , as measured by a thermo-coupling back sensor. Calibration using a test wafer showed the surface temperature of roughly -20°C . Finally, the surface of the Al layer was oxidized *in situ* for 10 s using 10 Torr partial oxygen pressure, converting the top 2 nm of Al into a uniform layer of approximately 3 nm AlOx.

For processing, the wafer was diced into $5 \times 5 \text{ mm}^2$ pieces. The devices were fabricated using standard electron beam lithography techniques. Al was selectively etched using a combination of AR 300-80 (new) adhesion promoter, CSAR 62 (AR-P 6200) 4% resist, and IPA:TMAH 0.2 N developer 19:1 solution with 6 min etching time at room temperature. Energy dispersive spectroscopy confirmed selective Al etching; see Fig S1. Normal metal Ti/Au (3/20 nm) leads were metalized using another layer of CSAR 62 (AR-P 6200) 4% resist.

MEASUREMENT SETUP

Transport measurements were performed using standard ac lock-in techniques in a dilution refrigerator with a base electron temperature of 40 mK, equipped with

a three-axis (1, 1, 6) T vector magnet. The dc lines used for addressing the devices were equipped with RF and RC filters, adding an additional line resistance of $R_{\text{line}} = 6.7 \text{ k}\Omega$. Two-terminal differential conductance measurements of the tunneling junctions were performed using $10 \mu\text{V}$ ac-voltage excitation at frequencies between 105 and 113 Hz. Four-terminal differential resistance measurements of the Al bars were carried out using a 10 nA ac-current excitation at frequencies between 13 and 44 Hz.

ADDITIONAL MEASUREMENTS

Four samples were investigated, each with several tunneling junctions and Al bars. The majority of the studied devices showed qualitatively similar behavior. Outliers were not considered, such as junctions with spurious spectral features hinting at inhomogeneous barriers and Al bars with inconsistent normal state resistance likely due to incomplete etching. The main findings are presented in the main text using representative data from Sample 1. Additional tunneling spectroscopy data from Sample 1 are summarized in Fig. S2. Fourteen junctions, with areas ranging from $120 \mu\text{m}^2$ to $6000 \mu\text{m}^2$, showed transition from normal to superconducting regime at $\mu_0 H = -(39 \pm 1) \text{ mT}$, and back to normal at $\mu_0 H = (71 \pm 1) \text{ mT}$, when sweeping from negative to positive H [Fig. S2(d)]. Here, the errors indicate the standard deviation across the investigated junctions.

Sample 2, nominally identical to Sample 1, showed qualitatively similar behavior. It had a slightly higher switching field to and from the superconducting regime and a narrower field range for percolative supercurrent, see Fig. S3(a-c). Fitting of the Usadel model to the tunneling spectra suggests that both the superconducting gap, Δ , and spin-flipping strength, Γ_{sf} , are approximately field-independent [Fig. S3(d)], consistent with literature [1]. The effective exchange spin splitting, h , displays a minimum at the coercive field around 15 mT, suggesting a switch in the average magnetization direction. The de-

duced spin-orbit strength, Γ_{so} , displays a lobe-shaped field dependence, with a sharp decrease around the coercive field, where accurate estimation becomes challenging due to the merging of the coherence peaks. The deduced paramagnetic limit $h_{\text{C}0} = \Delta/\sqrt{2} = (232 \pm 7) \mu\text{eV}$, with average Δ taken from the fit in Fig. S3(d). Fitting of the percolative model to the extracted average exchange splitting, $\langle h \rangle$, and zero-bias conductance yields $h_{\text{S}} = (320 \pm 60) \mu\text{eV}$, higher than for Sample 1, and $\xi/d = 9 \pm 7$, slightly smaller than for Sample 1 [Fig. S3(e) and (f)]. The errors were estimated by propagating the uncertainty in h_{C} in the model, giving a conservative upper bound. The magnetization curves deduced from the up and down H sweeps show residual paramagnetic behavior at high magnetic fields after they meet [Fig. S3(e)].

Atomic force microscopy (AFM) of the exposed EuS surfaces reveals significant differences in the topography of the two samples, see Fig. S4. The measured surface roughness, Rq , is (1.70 ± 0.04) nm for Sample 1, and (1.33 ± 0.05) nm for Sample 2, with the uncertainties given by the standard errors from independent measurements at different locations. We speculate that the different surface roughness leads to a different magnetic-domain formation dependence on the external magnetic field. The variations in surface topography between the two nominally identical samples are likely due to small thermal gradients across the wafer during the growth.

USADEL FIT PROCEDURE

Differential conductance of a normal metal–insulator–superconductor (NIS) tunneling junction is given by [2]

$$\frac{dI}{dV} = \frac{G_{\text{N}}}{n_{\text{N}}} \int_{-\infty}^{+\infty} n(\omega) [-\partial_{\omega} f(\omega - eV)] d\omega, \quad (\text{S1})$$

where G_{N} is the normal state conductance, e is the electron charge, n is the density of states in Al, $n_{\text{N}} = n(\omega \gg \Delta)$ is the normal density of states, $f(\omega, T)$ is the Fermi-Dirac distribution with temperature T and energy ω , and V is the bias voltage. Here and for the rest of the discussion, we set $\hbar = 1$.

We assume that, in general, a fraction x_{N} of the sample is in the normal state, while the rest remains in the superconducting phase with a pairing potential unaffected by orbital magnetism. In this case, the effective density of states in the Al film can be expressed as

$$n(\omega) = (1 - x_{\text{N}})n_{\text{S}}(\omega) + x_{\text{N}}n_{\text{N}}, \quad (\text{S2})$$

where $n_{\text{S}}(\omega)$ is the density of states of a homogeneous superconductor.

We model the spin-split superconductor with the Usadel equation [3], which has been extended for ferromagnet-superconductor heterostructures [4–6]. In the Usadel formalism, $n_{\text{S}}(\omega)$ can be defined using four parameters:

pairing potential Δ , average exchange splitting affecting the surviving superconducting regions $\langle h \rangle$, spin-flip relaxation rate due to magnetic impurities $\Gamma_{\text{sf}} = 3/2 \tau_{\text{sf}}^{-1}$, and spin-orbit scattering rate $\Gamma_{\text{so}} = 3/2 \tau_{\text{so}}^{-1}$, where τ_{sf} and τ_{so} are the spin-flip and spin-orbit scattering times. In general, Δ and $\langle h \rangle$ determine the position of the spin-split coherence peaks, Γ_{sf} broadens the peaks, while Γ_{so} affects the height difference between the peaks for the two spin components.

Fitting algorithm

The model is highly non-linear and thus requires a physically motivated fitting algorithm. We start by correcting any small voltage offset, defined by the middle of the superconducting gap, and by fixing the temperature to the base electron temperature of the dilution refrigerator, $T = 40$ mK [7]. We then fit the remaining parameters using the following steps.

1. Normal state conductance G_{N} .

The normal state conductance, G_{N} , is estimated by taking the average of the differential conductance at high voltage bias and large magnetic field, far above the Chandrasekar-Clogston limit [Fig. S5(a)].

2. Normal fraction x_{N} .

We estimate the normal fraction of the sample as $x_{\text{N}} \simeq G(V=0)/G_{\text{N}}$, assuming that the subgap tails of the coherence peaks due to thermal broadening are negligible [Fig. S5(b)]. We note that because of the uncertainty in G_{N} , the estimated x_{N} can be $\gtrsim 1$. Another reason G can exceed G_{N} can be attributed to the effect of quantum fluctuations above the paramagnetic limit [8]. Therefore, we constrain the values to range between 0 and 1, [Fig. S5(c)].

3. Usadel parameters.

For the remaining Usadel parameter, we explore two different fitting approaches.

For Sample 1, we first fit a single differential conductance trace at $\mu_0 H = 8$ mT, which we use to fix Γ_{sf} and Γ_{so} . We then fit the traces at other field values for Δ and $\langle h \rangle$. The results of this approach are summarized in Fig. S5(d).

For Sample 2, we run a free optimization routine, starting with the zero-field trace, followed by the fitting of $H > 0$ and then $H < 0$ data. The output from the previous fit is used as the initial guess for the next field value. The results of this approach are summarized in Fig. S3(d).

The two alternatives were chosen to ensure robustness in parameter estimation, particularly in scenarios where one of the two routines was prone to convergence issues. Cross-validation showed that

the results were consistent within acceptable error margins, reinforcing the reliability of using different approaches.

RESISTIVE NETWORK MODEL

Magnetic insulator

To better understand the observed experimental behavior, we introduce a simple theoretical model using the following experimentally-motivated considerations

1. Magnetic domains have a minimal size and behave as single spins. The size of these domains is distributed homogeneously enough to be described as a grid.
2. The micromagnetic configuration vector, \mathbf{m} , can only point in two anti-collinear directions, defined by the external magnetic field.
3. There is no spatial correlation between the magnetic grain orientations. We note that the spatial correlation is reintroduced in the superconductor via the averaging over ξ .

The probability of a domain pointing in the positive direction with respect to the sign of the magnetization is

$$p = \frac{1}{2} \left(1 + \frac{M}{M_S} \right), \quad (\text{S3})$$

where M is the total magnetization and M_S is the saturation magnetization. For a magnetic field sweep, we can generate a series of micromagnetic configurations, $m(H)$, whose average values relate to the extracted data by $\langle m(H) \rangle = M(H)/M_S = \langle h \rangle(H)/h_S$.

Superconductor

The response of a superconductor to a strong, non-uniform exchange field is highly nonlinear and nonlocal. A simple model to reproduce this complex superconducting response can be built by combining the following two operations. First, we define an averaging filter

$$K_\xi(\mathbf{r}) = \frac{1}{2\pi\xi^2} K_0(r/\xi), \quad (\text{S4})$$

where K_0 is the modified Bessel function of the second kind. The local average is then estimated with the convolution of the filter with the micromagnetic configuration, $\langle m \rangle_\xi = K_\xi(\mathbf{r}) \otimes m(\mathbf{r})$. This definition of K_ξ is motivated by the fact that both the spin-diffusion in the normal state and the linear response theory derived below are described by screened Poisson equations with fundamental solution in two dimensions given by Eq. (S4). In the

numerical implementation, the divergence of the filter at the origin is regularized by integrating numerically over the lattice.

Second, we introduce a local nonlinear operation to describe a step transition to the normal state at a given point within the superconductor if the local exchange splitting $\langle h \rangle_\xi$, as defined in the main-text Eq. (2), exceeds the paramagnetic limit h_C ; otherwise, it remains superconducting. Mathematically, we can describe the normal metallic regions as

$$X_n = \{ \mathbf{r} : \langle h \rangle_\xi > h_C \}, \quad (\text{S5})$$

which defines the normal fraction $x_N = |X_n|/L^2$ where L is the length of the simulation grid.

The effect of the two operations, namely the local averaging of micromagnetic configuration and the nonlinear transition to the normal state, is summarized in Fig. S6. It is apparent that for a given micromagnetic domain configuration, the sample turns normal in regions with one domain species but remains superconducting in regions with mixed domains.

Note that in the strong exchange field limit, where the local exchange field can reach values close to or higher than the paramagnetic limit, the superconducting behavior is nonlinear, as the spin-averaging length depends on the pairing potential. Therefore, local averaging through a convolutional filter can only serve as a qualitative representation of the physics of the structure.

Theoretical results of the percolation model

Before applying the model to the experimental data, we consider the possible zero-bias conductance curves predicted by the model.

In the limit of $g = 0$, there is no transition to the normal state if $h_S < h_C$, irrespectively from the other parameters. The normal state regions appear for $h_S > h_C$. In this case, the relationship between the spin-averaging length and the domain size determines the behavior of the system. For $\xi/d \ll 1$, there is effectively no averaging, and the sample is always in the normal state, with a potential exception of the domain-wall superconductivity. For $\xi/d \sim 1$, the finite local averaging results in a smooth transition. For $\xi/d \gg 1$, the transition to the normal state is sharp due to effective global averaging.

When $g \neq 0$, the Zeeman effect enables a local phase transition to the normal state even for $h_C > h_S$. We can quantify the importance of the Zeeman field by considering the critical field

$$H^* = \frac{h_{C0} - h_S}{g\mu_B\mu_0/2}. \quad (\text{S6})$$

Below H^* , the whole sample is superconducting as the total exchange splitting is not sufficient to suppress su-

perconductivity at any point. For $H > H^*$, the total exchange splitting can locally suppress superconductivity.

In this work, H^* is always negative due to $h_S > h_C$, suggesting that the Zeeman field plays a minor role. For the analysis, we fix $g = 2$ as we do not expect a strong renormalization of the electronic g factor in Al.

Model fitting

To apply the model to the experimental data, we first extract the magnetization curve $M(H)$ by fitting the main-text Eq. (3) to the measured sample average spin-splitting. The magnetization curve is then used to generate a collection of matching micromagnetic configurations, $\mathbf{m}(H)$, and calculate the evolution of the corresponding x_N . This step is repeated iteratively for various h_S and ξ/d values to minimize the residual sum of squares (RSS) between the predicted and experimentally determined x_N . The final results are shown in the main-text Fig. 3, while the value of $1/\text{RSS}$ is displayed in Fig. S7(a). A comparison between the predicted x_N evolutions in field for different values of h_S and ξ/d are shown in Fig. S7(b).

For the calculations shown in the main-text Fig. 4, we solve the continuity equation $\nabla \cdot \mathbf{j} = \nabla \cdot \rho^{-1} \nabla \varphi = 0$, where \mathbf{j} is the current density, ρ is the charge density, and φ is the electric potential. We apply a unit of voltage bias across neighboring domains and compute the resulting current flow to calculate the resistance.

USADEL MODEL DETAILS

In the time-reversed hole basis, $\psi = (\psi_\uparrow, \psi_\downarrow, -\psi_\downarrow, \psi_\uparrow)$, the Usadel equation for the quasiclassical propagator \check{g} in Matsubara representation reads as

$$D\nabla \cdot (\check{g}\nabla\check{g}) + [i\omega_n\tau_3\sigma_0 - i\mathbf{h} \cdot \boldsymbol{\sigma}\tau_3 - \check{\Delta} - \check{\Sigma}, \check{g}] = 0, \quad (\text{S7})$$

where D is the diffusion constant, $\omega_n = 2\pi\frac{(2n+1)}{T}$ with temperature T are the Matsubara frequencies, \mathbf{h} is the exchange splitting, $\check{\Delta} = \Delta\tau_1$ is the singlet order parameter and $\check{\Sigma}$ are additional self-energies [9]. We recall that the diffusion constant is defined as $D = v_F\ell/3$, where v_F is the Fermi velocity and ℓ is the elastic mean free path, while the coherence length for diffusive superconductor is $\xi = \sqrt{D/\Delta}$ [4–6]. The real-energy equation is obtained by the substitution $\omega_n \rightarrow -i\omega$. Eq. (S7) is complemented with the normalization constraint $\check{g}^2 = 1$.

To account for the spin-flipping scattering and spin-orbit coupling, we include the two spin-imbalance relaxation terms in the self-energy. The magnetic spin-flip term reads

$$\Sigma_{\text{sf}} = \frac{\boldsymbol{\sigma} \cdot \tau_3 \check{g} \boldsymbol{\sigma} \tau_3}{8\tau_{\text{sf}}}, \quad (\text{S8})$$

where τ_{sf} is related to normal state spin diffusion length by $\lambda_{\text{sf}} = \sqrt{\tau_{\text{sf}}D}$ [10]. The spin-orbit scattering term reads

$$\Sigma_{\text{so}} = \frac{\boldsymbol{\sigma} \cdot \check{g} \boldsymbol{\sigma}}{8\tau_{\text{so}}}. \quad (\text{S9})$$

After finding a solution for \check{g} , the local density of states is calculated as

$$n_S(\omega) = n_N \Re \text{tr}[\check{g}\tau_3\sigma_0], \quad (\text{S10})$$

where \Re denotes the real part.

Numerical method

To solve the Usadel equation, we adopt the hyperbolic (θ, \mathbf{M}) parametrization [11]. In this parametrization, the quasiclassical propagators reads

$$\check{g} = (\cos\theta M_0 + i\sin\theta \mathbf{M} \cdot \boldsymbol{\sigma})\tau_3 + (\sin\theta M_0 - i\cos\theta \mathbf{M} \cdot \boldsymbol{\sigma})\tau_1, \quad (\text{S11})$$

with $M_0^2 - \mathbf{M}^2 = 1$. With this, the Usadel equation can be split into a scalar (the $i\tau_2\sigma_0$ component) and a vector (the $\tau_2\boldsymbol{\sigma}$ component) coupled partial differential equations

$$D\nabla^2\theta + 2M_0(\Delta\cos\theta + i\omega\sin\theta) - 2\cos\theta\mathbf{h} \cdot \mathbf{M} - \frac{(2M_0^2 + 1)\sin(2\theta)}{4\tau_{\text{sf}}} = 0, \quad (\text{S12})$$

$$D(\mathbf{M}\nabla^2 M_0 - M_0\nabla^2 \mathbf{M}) + 2\mathbf{M}(\Delta\sin\theta - i\omega\cos\theta) - 2\sin\theta\mathbf{h}M_0 + \left[\frac{1}{\tau_{\text{so}}} + \frac{1}{2\tau_{\text{sf}}}\cos(2\theta)\right]M_0\mathbf{M} = 0. \quad (\text{S13})$$

We discretize Eqs. (S12) and (S13) using a finite-difference scheme and solve the nonlinear partial differential equations with the Newton method. The code for this procedure is provided in Ref. [12].

Spin-averaging length

To gain further insight into the behavior of a superconductor subjected to an inhomogeneous ferromagnetic proximity effect, we simplify the Usadel model for ana-

lytical treatment by following the methodology outlined in Ref. [13]. The homogeneous solution of the Usadel equations in the absence of self-energy scattering terms takes the form of

$$\check{g} = \frac{-i(\omega - \mathbf{h} \cdot \boldsymbol{\sigma})}{\sqrt{\Delta^2 - (\omega - \mathbf{h} \cdot \boldsymbol{\sigma})^2}} \tau_3 + \frac{\Delta}{\sqrt{\Delta^2 - (\omega - \mathbf{h} \cdot \boldsymbol{\sigma})^2}} \tau_1. \quad (\text{S14})$$

In the (θ, \mathbf{M}) parametrization, Eq. (S14) is given by

$$\tan \theta = \frac{i\Delta}{\omega}, \quad M_0 = 1, \quad \mathbf{M} = 0. \quad (\text{S15})$$

We consider a weak perturbation of the homogeneous solution, ensuring that θ and M_0 remain unaffected while the triplet vector experiences perturbation. By linearization, one can show that in the homogeneous case $\mathbf{M} = \frac{\mathbf{h}}{\Delta}$, which can be used to define the effective field $\tilde{\mathbf{h}} \equiv \Delta \mathbf{M}$ acting at a specific point.

In the inhomogeneous case, Eq. (S13) becomes

$$\frac{\mathbf{h}}{\Delta} = -\frac{1}{2} \frac{D}{\Delta} \sqrt{1 - \frac{\omega^2}{\Delta^2}} \nabla^2 \mathbf{M} + \mathbf{M} \left(1 - \frac{\omega^2}{\Delta^2}\right) + \frac{\sqrt{1 - \omega^2/\Delta^2}}{2\Delta} \left[\frac{1}{\tau_{\text{so}}} - \frac{1}{2\tau_{\text{sf}}} \frac{\Delta^2 + \omega^2}{\Delta^2 - \omega^2} \right] \mathbf{M}. \quad (\text{S16})$$

We can rearrange the equation as a screened Poisson par-

tial differential equation by defining a screening parameter

$$\alpha(\omega) = \left(1 - \frac{\omega^2}{\Delta^2}\right) + \frac{\sqrt{1 - \omega^2/\Delta^2}}{2\Delta} \left[\frac{1}{\tau_{\text{so}}} - \frac{1}{2\tau_{\text{sf}}} \frac{\Delta^2 + \omega^2}{\Delta^2 - \omega^2} \right], \quad (\text{S17})$$

and searching for the effective field $\tilde{\mathbf{h}}$

$$\left[-\frac{1}{2} \sqrt{1 - \omega^2/\Delta^2} \xi^2 \nabla^2 + \alpha(\omega) \right] \tilde{\mathbf{h}} = \mathbf{h}. \quad (\text{S18})$$

In two dimensions, the Green function of the homogeneous partial differential equation is

$$G(\mathbf{r}) = \frac{1}{2\pi} K_0(\mathbf{r}/\lambda), \quad (\text{S19})$$

where $\lambda = \xi \sqrt{\frac{\sqrt{1 - \omega^2/\Delta^2}}{2\alpha(\omega)}}$, such that the effective field is

$$\tilde{\mathbf{h}}(\mathbf{r}) = \int d\mathbf{r}' G(\mathbf{r} - \mathbf{r}') \frac{\mathbf{h}(\mathbf{r}')}{\alpha(\omega)}. \quad (\text{S20})$$

Therefore, the quantity λ can be identified as the spin-averaging length.

Surf. Sci. **94**, 100540 (2019).

* These authors contributed equally to this work.

- [1] A. Hijano, S. Ilić, M. Rouco, C. González-Orellana, M. Ilyn, C. Rogero, P. Virtanen, T. T. Heikkilä, S. Khorshidian, M. Spies, N. Ligato, F. Giazotto, E. Strambini, and F. S. Bergeret, Coexistence of superconductivity and spin-splitting fields in superconductor/ferromagnetic insulator bilayers of arbitrary thickness, *Phys. Rev. Res.* **3**, 023131 (2021).
- [2] I. Giaever and K. Megerle, Study of Superconductors by Electron Tunneling, *Phys. Rev.* **122**, 1101 (1961).
- [3] K. D. Usadel, Generalized Diffusion Equation for Superconducting Alloys, *Phys. Rev. Lett.* **25**, 507 (1970).
- [4] F. S. Bergeret, A. F. Volkov, and K. B. Efetov, Odd triplet superconductivity and related phenomena in superconductor-ferromagnet structures, *Rev. Mod. Phys.* **77**, 1321 (2005).
- [5] F. S. Bergeret, M. Silaev, P. Virtanen, and T. T. Heikkilä, Colloquium: Nonequilibrium effects in superconductors with a spin-splitting field, *Rev. Mod. Phys.* **90**, 041001 (2018).
- [6] T. T. Heikkilä, M. Silaev, P. Virtanen, and F. S. Bergeret, Thermal, electric and spin transport in superconductor/ferromagnetic-insulator structures, *Prog. Surf. Sci.* **94**, 100540 (2019).
- [7] F. Nichele, A. C. C. Drachmann, A. M. Whicar, E. C. T. O'Farrell, H. J. Suominen, A. Fornieri, T. Wang, G. C. Gardner, C. Thomas, A. T. Hatke, P. Krogstrup, M. J. Manfra, K. Flensberg, and C. M. Marcus, Scaling of majorana zero-bias conductance peaks, *Phys. Rev. Lett.* **119**, 136803 (2017).
- [8] M. Khodas, A. Levchenko, and G. Catelani, Quantum-Fluctuation Effects in the Transport Properties of Ultrathin Films of Disordered Superconductors above the Paramagnetic Limit, *Phys. Rev. Lett.* **108**, 257004 (2012).
- [9] F. Aikebaier, P. Virtanen, and T. Heikkilä, Superconductivity near a magnetic domain wall, *Phys. Rev. B* **99**, 104504 (2019).
- [10] J. P. Morten, A. Brataas, and W. Belzig, Spin transport in diffusive superconductors, *Phys. Rev. B* **70**, 212508 (2004).
- [11] D. A. Ivanov and Y. V. Fominov, Minigap in superconductor-ferromagnet junctions with inhomogeneous magnetization, *Phys. Rev. B* **73**, 214524 (2006).
- [12] A. Maiani, pyUsadel, Zenodo, (2023); 10.5281/zenodo.8264498.
- [13] A. Hijano, V. N. Golovach, and F. S. Bergeret, Quasiparticle density of states and triplet correlations in superconductor/ferromagnetic-insulator structures across a sharp domain wall, *Phys. Rev. B* **105**, 174507 (2022).

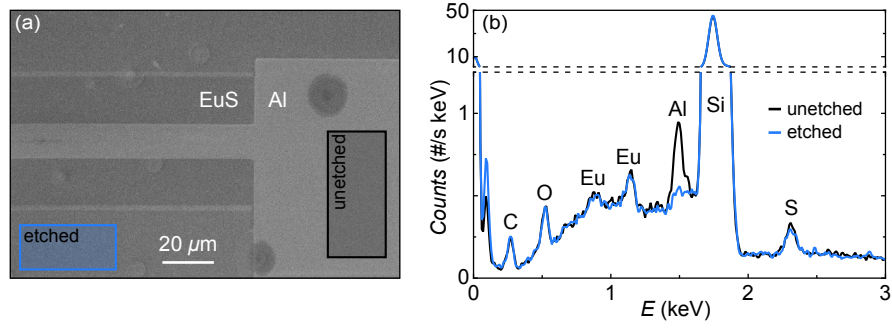


FIG. S1. (a) Scanning electron micrograph of a test chip after Al etching. Exposed EuS (etched regions) appear darker, whereas the unetched Al appears brighter. (b) Comparison of two energy dispersive spectra integrated over two areas [indicated in (a)] with etched and unetched Al. The main difference between the two spectra is the suppressed Al peak for the etched area, whereas the Eu and S peaks remain nearly unchanged.

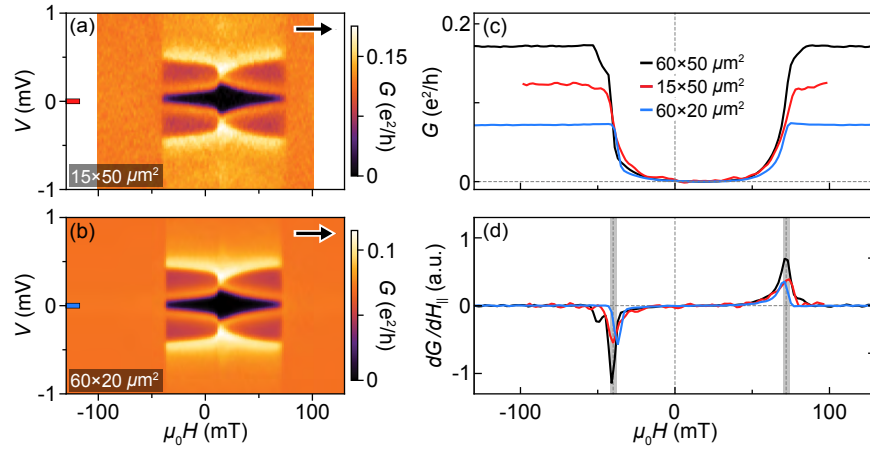


FIG. S2. (a) Differential conductance, G , as a function of voltage bias, V , and in-plane magnetic field, H , for $15 \times 50 \mu\text{m}^2$ tunneling junction on Sample 1. Sweep direction is indicated by the arrow. (b) Same as (a) but for $60 \times 20 \mu\text{m}^2$ junction. (c) Zero-bias G line-cuts taken from (a), (b), and main-text Fig. 1(d). (d) Same as (c) but numerically differentiated with respect to H . Black dashed lines indicate transitions from normal to superconducting regime at $\mu_0 H = -(39 \pm 1)$ mT and back to normal at $\mu_0 H = (71 \pm 1)$ mT. The gray bands represent errors from standard deviation across the junctions.

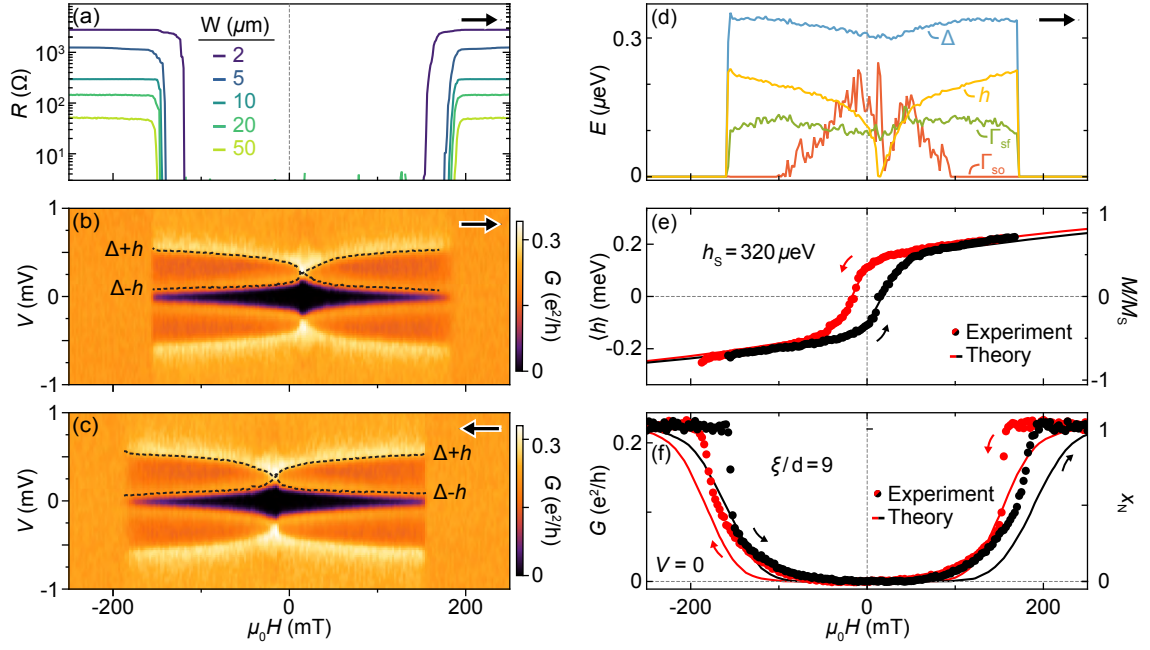


FIG. S3. (a) Differential resistance, R , as a function of in-plane magnetic field, H , for Al bars of different widths on Sample 2. Sweep direction is indicated by the arrow. Data for 2, 5, and 50 μm bars were taken in a three-terminal configuration. Background resistance was subtracted using a five-point average around $H = 0$. (b) Differential conductance, G , as a function of voltage bias, V , and H for $25 \times 50 \mu\text{m}^2$ tunneling junction on Sample 2. (c) Same as (b) but for opposite field-sweep direction. (d) Output of the Usadel fitting routine performed on data in (b), giving superconducting gap, Δ , effective exchange splitting, h , spin-flip relaxation rate, Γ_{sf} , and spin-orbit scattering rate, Γ_{so} . (e) and (f) Results of the percolative model. (e) Average exchange splitting, $\langle h \rangle$, (left axis) and fitted magnetization normalized to its saturation value, M/M_S , (right axis) as a function of $\mu_0 H$. The fit yields paramagnetic limit $h_C = 230 = \Delta/\sqrt{2} = (232 \pm 7) \mu\text{eV}$. (f) Zero-bias conductance, G , (left axis) taken from (b) and (c), and deduced normal fraction of the sample, x_N , (right axis) as a function of H . The fit yields saturation spin-splitting $h_S = 320 \mu\text{eV}$ and the ratio between the coherence length and minimal domain size, $\xi/d = 9$.

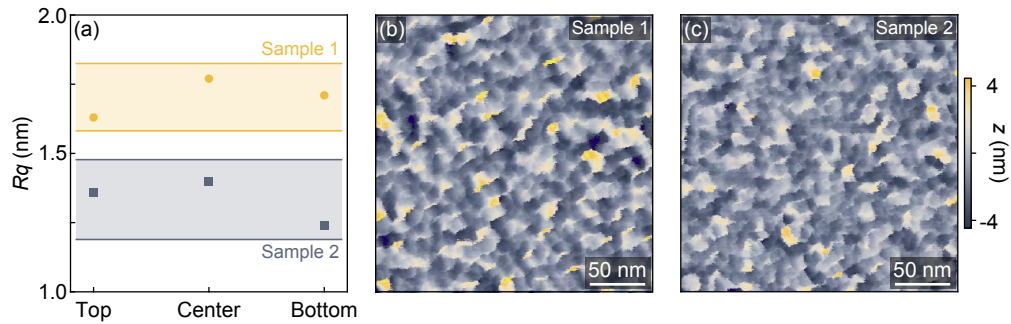


FIG. S4. (a) Surface roughness, Rq , measured on the exposed EuS surface at three different locations for both samples. (b) Atomic force micrograph taken at the bottom of Sample 1, with $Rq = 1.7 \text{ nm}$. (c) Same as (b) but taken at the center of Sample 2, with $Rq = 1.4 \text{ nm}$.

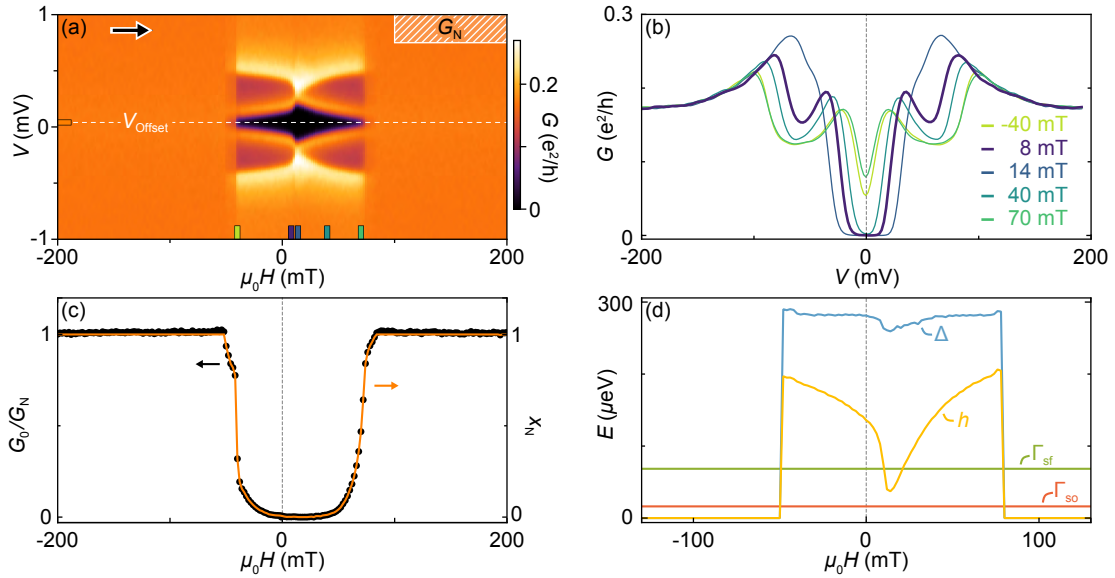


FIG. S5. Illustration of the Usadel fitting algorithm steps applied to the data shown in the main-text Fig. 1(d). (a) and (b) After correcting the voltage-bias offset, V_{Offset} , we extract the normal state conductance, G_N , by taking the average of a region at high field and bias. (c) Next, we extract the fraction of the sample in the normal state, x_N , defined as $G(V=0)/G_N$, constrained to range between 0 and 1. (d) Finally, we fit the data for the Usadel parameters: pairing potential Δ , average exchange splitting $\langle h \rangle$, spin-flip relaxation rate Γ_{sf} , and spin-orbit scattering rate Γ_{so} .

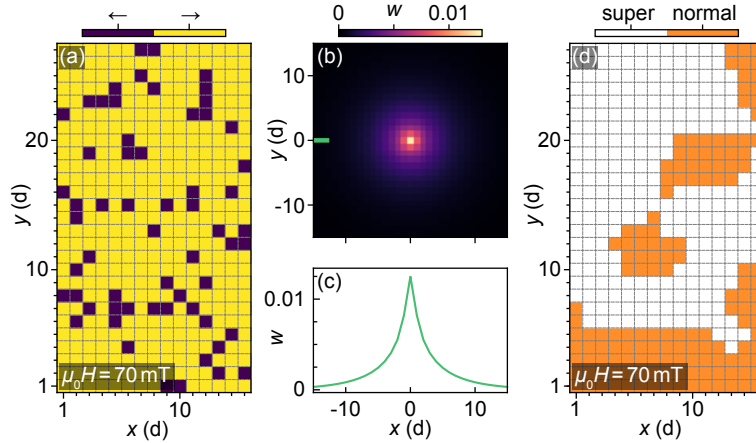


FIG. S6. (a) Zoom-in micromagnetic domain configurations of the grid taken from a $200 d \times 1000 d$ realization at in-plane magnetic field $\mu_0 H = 70$ mT. (b) and (c) Averaging filter weight, w , calculated using Eq. (S4) with $\xi/d = 13$. (d) Spatial distribution of the superconducting (white) and normal (orange) regions, calculated by applying the averaging filter to the micromagnetic configuration in (a). The grid turns normal where local average spin-splitting exceeds paramagnetic limit $\langle h \rangle_\xi > h_C$.

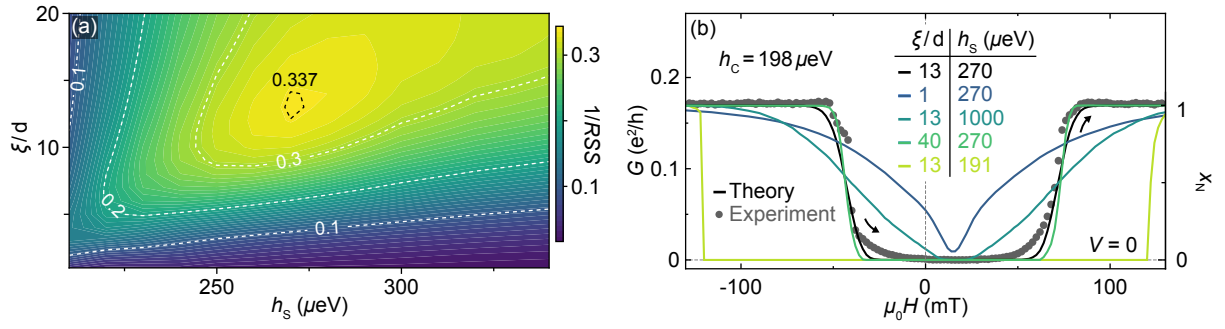


FIG. S7. (a) Inverse of the residual sum of squares, $1/\text{RSS}$, as a function of saturation exchange splitting, h_s , and the ratio between the superconducting coherence length and minimal domain size, ξ/d . The data were calculated using the minimal model for zero-bias conductance to compare the predicted and experimentally determined normal fraction of the sample, x_N , shown in the main-text Fig. 3(d). (b) A comparison between the predicted x_N evolutions with in-plane field H for different values of h_s and ξ/d .